J Eng Math (2007) 58:251–265
DOI 10.1007/s10665-006-9109-3

ORIGINAL PAPER

On Helmholtz and higher-order resonance of twin floating bodies

Ronald W. Yeung · Robert K. M. Seah

Received: 6 February 2006 / Accepted: 22 August 2006 / Published online: 16 January 2007

Abstract The Helmholtz mode and other symmetric modes of resonance of a moonpool between two heaving rectangular floating cylinders are investigated. The hydrodynamic behavior around these resonant modes is examined together with the associated mode shapes in the moonpool region. It is observed that near each of the resonance frequencies, the damping coefficient can vanish. The Helmholtz mode is characterized by a region of modest variation of added-mass value from negative to positive near the Helmholtz frequency. The peaks are, however, bounded with the cross-over point in sign corresponding to a bounded spike in damping. The higher-order resonant modes are characterized by the presence of standing waves in the moonpool, which leads to large spikes in the hydrodynamic behavior near the resonance frequencies. The Helmholtz frequency has a distinct value, while the higher-order resonances occur at fairly regular intervals of the frequency parameter, $\sigma^2(w-b)/g$, where $w-b$ is the moonpool gap. The parametric dependence of the hydrodynamic behavior on frequency and geometry is discussed.

Keywords Catamarans · Helmholtz resonance · Hydrodynamic coefficients · Moonpool · Twin hulls

With best wishes to my colleague and good friend, Nick Newman, on the occasion of his 70th birthday. A leader and staunch supporter of marine hydrodynamics, Nick has expanded the reach and influence of this field through his insights and publications. His contributions have been wide-ranged and his graciousness to young researchers is exemplary. May he enjoy the best of health in the years to come.

R.W. Yeung

1 Introduction

This paper aims to study and understand the resonance frequencies and free-surface modal shapes between two heaving floating bodies. Such a geometry occurs in twin hulls or similar structures with "moonpools". It also examines the behavior of the hydrodynamic coefficients in the frequency domain around the resonance. Of particular interest is the Helmholtz mode which has a non-zero mean elevation in the gap or moonpool region. It is sometimes referred to as the pumping or piston mode.

R. W. Yeung (✉) · R. K. M. Seah
Department of Mechanical Engineering, University of California at Berkeley,
Berkeley, CA 94720-1740, USA
e-mail: rwyeung@berkeley.edu

With some exceptions, the hydrodynamic coefficients of a single body, floating or submerged, normally are fairly monotonic functions of frequency. The presence of a moonpool offers the possibility of internal resonances, which will alter the behavior of these coefficients dramatically. One of the earliest works on this behavior was due to Wang and Wahab [1] who studied, numerically and experimentally, pairs of floating circular cylinders with varying lateral separations. They identified a Helmholtz mode, which they referred to as the "zeroth" mode, as well as a sequence of higher-order resonant modes. Marthinsen and Vinje [2] utilized matched asymptotic expansions to study a narrow gap between two rectangular bodies. Miles [3] and Miles and Lee [4] used an equivalent circuit analysis to predict the Helmholtz response of a harbor to exterior excitations. Ünlüata and Mei [5] similarly studied harbor oscillations as a boundary-value problem.

In search of probable homogeneous solutions of these frequency-domain problems, McIver [6] derived shapes of a twin body which exhibited a "trapped-mode" frequency, at which no waves are radiated to infinity. Further studies of related shapes in three dimensions were made by McIver and McIver [7], and Newman [8], the latter investigating a shape in toroidal form. These trapped modes are characterized by zero wave radiation together with infinite added-mass coefficients. In frequency-domain computations, the trapped-mode frequency shows up as an unbounded solution since the multiplier on the homogeneous solution is non-unique. The existence of shapes of a single body that has vanishingly small damping has also been known for a long time since the 1960s [9]. Kyozuka and Yoshida [10] in fact derived the streamlines for axisymmetric bodies that have zero damping, hence zero wave-exciting force. However, the solution, and hence the added-mass coefficient, is bounded at these radiation-free frequencies.

Among others, the method of matched eigenfunctions has been used by Garrett [11], who studied the diffraction of a "bottomless harbor". Yeung [12] further developed the method to examine the hydrodynamic coefficients of a truncated vertical cylinder. A similar procedure was used by Miloh [13] to investigate the wave load on a solar pond that contains a two-layer fluid. Similarly, Shipway and Evans [14] investigated the trapped modes of concentric cylinders with thin walls. More recently, Mavrakos [15] extended this last study to determine the hydrodynamic coefficients of concentric cylinders with walls of finite thicknesses. The eigenfunction-matching method is efficient, accurate, and most importantly, free of the occurrence of irregular frequencies typically encountered in integral-equation formulations.

Modal shapes within the moonpool area were addressed by Molin [16], who modeled the presence of the body as a laterally unbounded plate on the free surface. Shipway and Evans [14] provided a selection of wave forms for the trapped modes between concentric cylinders. Not as much is known about how the modal shapes and the hydrodynamic coefficients behave across the resonance frequencies.

After developing the solution of the problem in the next section, we examine how the hydrodynamic properties depend on the geometric parameters of the cylinders. We then discuss how the free surface will vary with the type of resonance mode.

2 Formulation and analysis

The method of analysis follows closely that used in [12]. A pair of infinitely long parallel cylinders of identical rectangular profiles as shown in Fig. 1 is assumed to oscillate vertically in the free surface of water of depth h. Each cylinder has a beam of $2b$ and a draft of d. The gap between the pair is $2(w - b)$, where $2w$ is the distance between the centerlines of each of the cylinders.

Since only heave motion is considered here, the solution is symmetric about $x = 0$ and only the two-dimensional domain $x \geq 0$ is considered. With the usual assumption that the fluid is incompressible and inviscid, and the flow irrotational, the following linearized boundary-value problem based on a small amplitude of motion ζ_2 is well described in [17].

Let the heave motion of both cylinders be described by $\zeta_2 \cos \sigma t$, σ being the angular frequency; then the velocity potential within the fluid can be written as

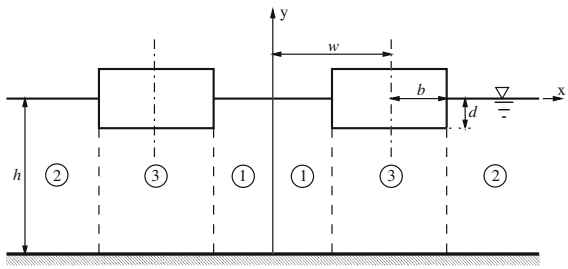

Fig. 1 Schematic of the fluid domain

$$\Phi(x,y,t) = \mathfrak{Re}[-\mathbf{i}\sigma\zeta_2\phi(x,y)\mathrm{e}^{-\mathbf{i}\sigma t}], \tag{1}$$

where $\phi(x,y)$ is the so-called unit (-amplitude) spatial potential. The governing equation for ϕ is Laplace's equation:

$$\nabla^2\phi = 0, \tag{2}$$

where ϕ must satisfy also the no-flux conditions on the solid boundaries:

$$\phi_x(x = w \pm b, y) = 0, \quad \text{for } y \geq -d, \quad \phi_y(x, y = -h) = 0. \tag{3}$$

Symmetry of the solution implies

$$\phi_x(0,y) = 0, \tag{4}$$

and the kinematic boundary condition at bottom of the cylinder gives,

$$\phi_y(x, y = -d) = 1 \quad \text{for } w - b \leq x \leq w + b. \tag{5}$$

The linearized free-surface boundary condition is applied at $y = 0$,

$$\phi_y - \nu\phi = 0, \tag{6}$$

where $\nu = \sigma^2/g$. Finally, the potential also has to satisfy an "outgoing-wave" condition far from the cylinders.

2.1 Division of fluid domain

The domain of the analysis is split into three distinct rectangular sub-domains with different types of spatial variation of the potential in each. These potentials are denoted by ϕ^i, ϕ^{e1}, and ϕ^{e2}. ϕ^i is the potential of the subdomain (Region 3 in Fig. 1) underneath the cylinder ($w - b \leq x \leq w + b$) and above the sea floor ($-h \leq y \leq -d$). Thus, the fluid within this subdomain obeys the governing equation

$$\nabla^2\phi^i = 0, \tag{7}$$

and the following boundary conditions:

$$\phi^i_y = 1 \quad \text{for } w - b \leq x \leq w + b,\ y = -d, \tag{8}$$
$$\phi^i_y = 0 \quad \text{for } w - b \leq x \leq w + b,\ y = -h, \tag{9}$$
$$\phi^i = \phi^{e1} \quad \text{for } x = w - b,\ -h \leq y \leq -d, \tag{10}$$
$$\phi^i = \phi^{e2} \quad \text{for } x = w + b,\ -h \leq y \leq -d. \tag{11}$$

Equations 8 and 9 are the body and no-flux boundary conditions, respectively. Equations 10 and 11 express the requirement of matching the potential (or linearized fluid pressure) at the juncture boundaries shared by the subdomains.

The functions ϕ^{e1} and ϕ^{e2} are the potentials of the inner and outer fluid subdomains in Regions 1 and 2, respectively. They satisfy the governing equation,

$$\nabla^2\phi^q = 0, \quad q = e1,\ e2, \tag{12}$$

and the following set of boundary conditions:

$$\phi^q_y = 0, \tag{13}$$
$$\phi^q_y - \nu\phi^q = 0, \tag{14}$$
$$\phi^q_x = 0, \tag{15}$$
$$\phi^q_x = \phi^i_x. \tag{16}$$

Equations 13–15 follow from the original problem of ϕ. However, (16) is needed to ensure continuity of fluid fluxes at the juncture boundaries. This complements (10) and (11) mentioned above for these same boundaries. In addition, symmetry about $x = 0$ for Region 1 gives

$$\phi^{e1}_x = 0 \quad \text{for } x = 0, \quad -h \le y \le 0, \tag{17}$$

while in Region 2 the radiation condition for wave elevation $Y(x,t)$ implies

$$Y(x,t) = \zeta_2 A_2 \mathrm{e}^{(\mathbf{i}m_0 x - \mathbf{i}\sigma t)} = \zeta_2\eta(x)\mathrm{e}^{-\mathbf{i}\sigma t}, \quad \text{as } x \to \infty. \tag{18}$$

Here, A_2 is the wave amplitude per unit ζ_2, $\eta(x)$ the free-surface profile, and m_0 a wave number. The solutions in all three regions must be properly matched.

2.2 Solution of ϕ^i

In Region 3, ϕ^i can be decomposed into a homogeneous solution ϕ^{ih} and a particular solution ϕ^{ip}, with the latter constructed to satisfy inhomogeneous boundary condition, Eq. 8:

$$\phi^i = \phi^{ih} + \phi^{ip}. \tag{19}$$

The particular solution subject to (8) and (9) can be shown easily to be:

$$\phi^{ip} = \frac{1}{2(h-d)}\left[(y+h)^2 - (x-w)^2\right]. \tag{20}$$

The homogeneous solution is subject to

$$\phi^{ih}_y = 0, \ \text{ for } y = -d, \quad \text{and } y = -h. \tag{21}$$

This yields the eigenvalues

$$\gamma_n = \frac{n\pi}{h-d}, \quad n = 0, 1, \ldots \tag{22}$$

with ϕ^{ih} being defined by

$$\phi^{ih} = \sum_{n=0}^{\infty}(C_{1n}X_{1n}(x) + C_{2n}X_{2n}(x))Y^i_n(y), \tag{23}$$

where

$$X_{1n} = \begin{cases} 1 & \text{for } n = 0, \\ \cosh\gamma_n(x-w)/\cosh\gamma_n b & \text{for } n \ge 1, \end{cases} \tag{24}$$

$$X_{2n} = \begin{cases} (x-w)/b & \text{for } n = 0, \\ \sinh\gamma_n(x-w)/\sinh\gamma_n b & \text{for } n \ge 1, \end{cases} \tag{25}$$

and

$$Y_n^i = \begin{cases} 1 & \text{for } n = 0, \\ \sqrt{2}\cos\gamma_n(y+h) & \text{for } n \geq 1. \end{cases} \tag{26}$$

Here, Y_n^i is constructed as an orthonormal set so that the following inner product can be defined for any combination of l and m:

$$\langle Y_l^i, Y_m^i \rangle \equiv \frac{1}{h-d}\int_{-h}^{-d} Y_l^i(y) Y_m^i(y)\mathrm{d}y = \delta_{lm}. \tag{27}$$

If the expressions for ϕ^{ip} and ϕ^{ih} are introduced into the matching boundary conditions at $x = w - b$ and $x = w + b$, the unknown coefficients C_{1n} and C_{2n} can be related to the potentials ϕ^{e1} and ϕ^{e2}.

$$C_{1n} - C_{2n} = \langle \phi^{e1}, Y_n^i \rangle - \langle \phi^{ip}, Y_n^i \rangle \quad \text{at } x = w - b, \tag{28}$$

$$C_{1n} + C_{2n} = \langle \phi^{e2}, Y_n^i \rangle - \langle \phi^{ip}, Y_n^i \rangle \quad \text{at } x = w + b. \tag{29}$$

This result was facilitated by using the orthogonality condition (27).

2.3 Solutions of ϕ^{e1} and ϕ^{e2}

Solution for these regions can written as:

$$\phi^q = \sum_{k=0}^{\infty} B_k^q \Lambda_k^q(x) Y_k^e(y), \tag{30}$$

where Λ_k^q and Y_k^e are defined by

$$\begin{aligned} \Lambda_k^{e1} &= \begin{cases} \cos m_0 x / \cos m_0(w-b) & \text{for } k = 0, \\ \cosh m_k x / \cosh m_k(w-b) & \text{for } k \geq 1, \end{cases} \\ \Lambda_k^{e2} &= \begin{cases} e^{\mathbf{i}m_0(x-(w+b))} & \text{for } k = 0, \\ e^{-m_k(x-(w+b))} & \text{for } k \geq 1, \end{cases} \end{aligned} \tag{31}$$

and

$$Y_k^e = \begin{cases} \cosh m_0(y+h)/N_0^{\frac{1}{2}} & \text{for } k = 0, \\ \cos m_k(y+h)/N_k^{\frac{1}{2}} & \text{for } k \geq 1. \end{cases} \tag{32}$$

Here, m_k are eigenvalues that result from Eqs. 13 and 14 (see [17]):

$$m_0 \tanh m_0 h = \nu, \quad m_k \tan m_k h = -\nu, \quad k = 1, 2, \ldots \tag{33}$$

and N_k are scale factors:

$$N_k = \begin{cases} \frac{1}{2}\left[1 + \sinh(2m_0 h)/(2m_0 h)\right] & \text{for } k = 0, \\ \frac{1}{2}\left[1 + \sin(2m_k h)/(2m_k h)\right] & \text{for } k \geq 1. \end{cases} \tag{34}$$

which are introduced so that the vertical modes Y_k^e form an orthonormal set:

$$\langle Y_k^e, Y_j^e \rangle \equiv \frac{1}{h}\int_{-h}^{0} Y_k^e(y) Y_j^e(y)\mathrm{d}y = \delta_{kj}. \tag{35}$$

Again, the unknown coefficients B_k^q can be related to the interior coefficients C_{1n} and C_{2n} by using matching boundary conditions at $x = w \pm b$, but this time to satisfy flux continuity:

$$\sum_{k=0}^{\infty} B_k^q \Lambda_k^{q\prime} Y_k^e = \begin{cases} 0 & \text{for } y \geq -d, \\ \phi_x^i & \text{for } -h \leq y < -d. \end{cases} \tag{36}$$

Here and henceforth, all Λ_k^q and $\Lambda_k^{q'}$ are understood to be evaluated at $x = w \pm b$, for $q = e1, e2$, respectively. When (35) is used on (36), the coefficients B_k^q can be promptly expressed in terms of ϕ^{ih} and ϕ^{ip}.

$$B_k^q \Lambda_k^{q'} = \frac{1}{h} \int_{-h}^{-d} \phi_x^{ih} Y_k^e \mathrm{d}y + B_k^{q*}, \tag{37}$$

where

$$B_k^{q*} = \frac{1}{h} \int_{-h}^{-d} \phi_x^{ip} Y_k^e \mathrm{d}y. \tag{38}$$

2.4 Matching of solutions

Equations 28, 29, and 37 represent a system of equations with four sets of complex unknowns C_{1n}, C_{2n}, B_k^{e1}, and B_k^{e2}. To simplify this system, B_k^{e1} and B_k^{e2} need to be expressed in terms of C_{1n} and C_{2n} or vice versa. The expansion of ϕ^{e1} can be introduced into Eq. 28, which results in

$$C_{1n} - C_{2n} = \frac{1}{h-d} \int_{-h}^{-d} \left[\sum_{k=0}^{\infty} B_k^{e1} \Lambda_k^{e1} Y_k^e \right] Y_n^i \mathrm{d}y - \langle \phi^{ip}, Y_n^i \rangle. \tag{39}$$

Upon evaluation, it yields

$$C_{1n} - C_{2n} = \frac{1}{h-d} \sum_{k=0}^{\infty} B_k^{e1} \Lambda_k^{e1} S_{kn} - \langle \phi^{ip}, Y_n^i \rangle, \tag{40}$$

where

$$S_{kn} = \begin{cases} \sinh m_0(h-d)/m_0 N_0^{\frac{1}{2}} & \text{for } k = 0,\ n = 0, \\ \sin m_k(h-d)/m_k N_k^{\frac{1}{2}} & \text{for } k \geq 1,\ n = 0, \\ \sqrt{2} m_0 (-1)^n \sinh m_0(h-d)/N_0^{\frac{1}{2}} (m_0^2 + \gamma_n^2) & \text{for } k = 0,\ n \geq 1, \\ \sqrt{2} m_k (-1)^n \sin m_k(h-d)/N_k^{\frac{1}{2}} (m_k^2 - \gamma_n^2) & \text{for } k \geq 1,\ n \geq 1. \end{cases} \tag{41}$$

Similarly, ϕ^{ih} can be introduced into Eq. 37, which gives

$$B_k^{e1} = \left(\Lambda_k^{e1'} \right)^{-1} \left\{ \frac{1}{h} \sum_{n=0}^{\infty} \left[C_{1n} X_{1n}{}' + C_{2n} X_{2n}{}' \right] S_{kn} + B_k^{e1*} \right\}. \tag{42}$$

Equation 42 can now be inserted into (40) and the result can be rearranged so that the known terms are on the right,

$$C_{1n} - C_{2n} - \frac{1}{h(h-d)} \sum_{k=0}^{\infty} \sum_{j=0}^{\infty} \frac{\Lambda_k^{e1}}{\Lambda_k^{e1'}} S_{kn} S_{kj} \left[C_{1j} X_{1j}{}' + C_{2j} X_{2j}{}' \right] = \frac{1}{h-d} \sum_{k=0}^{\infty} \frac{\Lambda_k^{e1}}{\Lambda_k^{e1'}} S_{kn} B_k^{e1*} - \langle \phi^{ip}, Y_n^i \rangle |_{x=w-b}. \tag{43}$$

The analogous equations to (43) and (42) for ϕ^{e2}, similarly obtained, are respectively:

$$C_{1n} + C_{2n} - \frac{1}{h(h-d)} \sum_{k=0}^{\infty} \sum_{j=0}^{\infty} \frac{\Lambda_k^{e2}}{\Lambda_k^{e2'}} S_{kn} S_{kj} \left[C_{1j} X_{1j}{}' + C_{2j} X_{2j}{}' \right] = \frac{1}{h-d} \sum_{k=0}^{\infty} \frac{\Lambda_k^{e2}}{\Lambda_k^{e2'}} S_{kn} B_k^{e2*} - \langle \phi^{ip}, Y_n^i \rangle |_{x=w+b}, \tag{44}$$

and

$$B_k^{e2} = \left(\Lambda_k^{e2'} \right)^{-1} \left\{ \frac{1}{h} \sum_{n=0}^{\infty} \left[C_{1n} X_{1n}{}' + C_{2n} X_{2n}{}' \right] S_{kn} + B_k^{e2*} \right\}. \tag{45}$$

In conclusion, Eqs. 43 and 44 now form a solvable set of linear equations of rank $2n$. The only unknowns in them are C_{1n} and C_{2n}. Once C_{1n} and C_{2n} have been determined, B_k^q follow from (42) and (45). It is of interest to note that $\Lambda_0^{e1\prime} = -m_0 \tan m_0(w-b)$ in (42), vanishes when the argument of tangent is an integer multiple of π. However, $B_0^{e1}\Lambda_0^{e1\prime}$ was found to remain bounded.

2.5 Determination of hydrodynamic coefficients

The non-dimensional heave hydrodynamic coefficients for a *twin* cylinder can be easily obtained from the velocity potential on the body using the following definition:

$$\mu_{22} + \mathbf{i}\lambda_{22} = \frac{2}{b^2}\int_{w-b}^{w+b} \phi^i(x,-d)\phi_y^i \mathrm{d}x = \frac{2}{b^2}\int_{w-b}^{w+b} \left[\phi^{ip} + \phi^{ih}\right] \mathrm{d}x. \tag{46}$$

Then, straight-forward integration yields the following final expression:

$$\mu_{22} + \mathbf{i}\lambda_{22} = \frac{2(h-d)}{b} - \frac{2}{3}\frac{b}{h-d} + \frac{4}{b}C_{10} + \frac{2^{5/2}}{b}\sum_{n=1}^{\infty}\frac{\cos\gamma_n(h-d)\tanh\gamma_n b}{\gamma_n b}C_{1n}. \tag{47}$$

Here, the dimensional added-mass and damping coefficients have been non-dimensionalized by ρb^2 and $\rho\sigma b^2$, respectively.

3 Behavior of hydrodynamic coefficients

Verification of the current solution was performed by comparing the heave hydrodynamic coefficients with results of Yeung [18] using an infinite-fluid source integral-equation method, as well as the earlier work of Fotsch [19] on a single cylinder. The twin-cylinder configuration reproduces single-cylinder results when the gap-to-draft ratio was taken to be small (2.0×10^{-5}).

In the computations reported here, the truncation of the series in (43) and (44) was taken at 50 terms, adequate to at least one place in the third digit for added mass and damping. However, in free-surface-elevation computations, 100 terms were often needed to achieve a good definition of the wave profile, especially near the body and free-surface intersection. This is to be expected, since we expect more terms in the series expansion will be needed in local quantities.

3.1 Behavior near Helmholtz frequency $(\nu b)_0$

Figure 2 shows the heave hydrodynamic coefficients of the twin cylinders as functions of νb in relatively deep water ($h/d = 20$). Results from the present solution are plotted together with those from the integral-equation solution method ([18], $h = \infty$). The good agreement of the two solutions is evident, except in the low-frequency area. The difference there is explained by the fact that μ_{22} approaches a constant in finite water depth [20–22], whereas its deep-water counterpart behaves like $\log(\nu b)$ (see [23]).

Of particular interest in this figure are critical frequencies where the damping vanishes. At these points, there will be persistent fluid motion with no dissipation. In the neighborhood of each point, at a slightly lower frequency, drastic changes in the hydrodynamic behavior always occur. It is helpful to assign a mode index using this zero-damping point, since frequencies at which maximum moonpool elevation occurs would depend on where the elevation is taken.

For this geometry, the Helmholtz mode can be identified at $(\nu b)_0 = 0.2617$, at which no radiating waves are generated by the heave oscillation since $\lambda_{22} = 0$; μ_{22} varies from negative values to positive values in this neighborhood. Two other critical frequencies, $(\nu b)_1 = 0.829$ and $(\nu b)_2 = 1.577$, are also seen. In

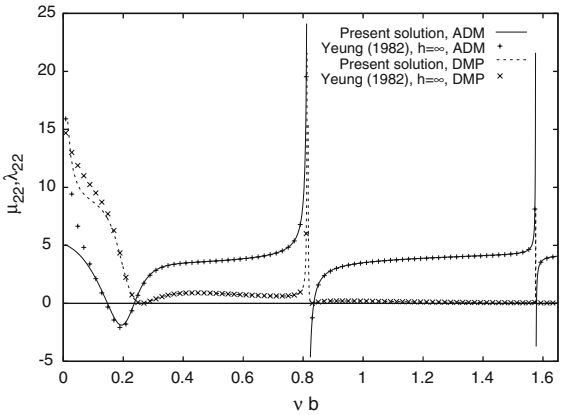

Fig. 2 Heave hydrodynamic coefficients for *twin* cylinders, $b/d = 1.0$, $w/b = 5.0$, $h/d = 20$

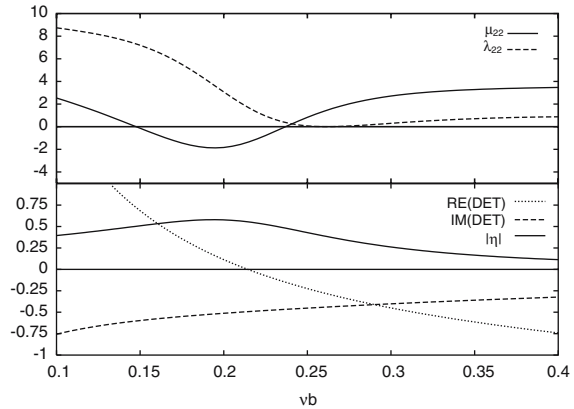

Fig. 3 Heave hydrodynamic coefficients at the Helmholtz resonance, shown with determinant of (43) and (44) and wave elevation averaged over moonpool $|\bar{\eta}|$, $b/d = 1.0$, $w/b = 5.0$

contrast, these higher-order modes are characterized by a spiky damping and added-mass behavior around the frequencies where damping vanishes. As will be illustrated later, the higher-order resonances correspond to oscillatory wave forms in the moonpool region. The modest behavior of μ_{22} at $(\nu b)_0$ makes it distinctively different from the other symmetric resonances.

Figures 3 and 4 compare the behavior of the complex determinant, associated with the unknown coefficients C_{1n} and C_{2n} in (43) and (44). The real and imaginary components of the determinants were multiplied by 10^{-89} and 10^{+12}, respectively, before being plotted in Figs. 3 and 4.

Also plotted in these figures is the modulus of the complex moonpool wave elevation, $|\bar{\eta}|$, spatially averaged over the moonpool. For the Helmholtz mode shown in Fig. 3, the location where the real component of the determinant crosses the axis ($\nu b = 0.218$) coincides with neither the maximum moonpool elevation ($\nu b = 0.193$) nor the zero damping location, $(\nu b)_0$. In contrast, for the first resonance seen in Fig. 4, the real component of the determinant crosses the axis very close to, but not exactly at, the peak moonpool elevation at $\nu b = 0.815$. Similar behavior was observed for resonances of higher order.

The frequency range in Fig. 4 has been greatly expanded to elucidate the behavior of the hydrodynamic coefficients around the resonance. Note that the vertical ordinates have been compressed. It is now evident that the seemingly large spike in the coefficients of Fig. 2 actually behaves in a smooth and bounded manner. The boundedness of the coefficients is related to the fact that the imaginary component of the determinant remains non-zero when the real component crosses the axis, resulting in a non-singular matrix.

The spike in the damping generally correlates well with the location of the abscissa crossover of the added-mass coefficient (rather than at the zero crossing of the real component of the determinant). This is especially evident for the $w/b = 1.5$ case, in Fig. 5, where the zero values for the added-mass coefficient and the real part of the determinant occurs at $\nu b = 0.510$ and 0.522, respectively. Here, the Helmholtz marker for zero-damping occurs at $(\nu b)_0 = 0.608$. The inter-relationship between the spike in damping, the change in sign of the added mass and the zero-damping location, or vice versa, should be deducible from the Kramers–Kronig relations.

As was stated previously, the critical frequencies are defined in this paper where the damping coefficients are zero. Figure 6 shows the damping coefficients for the previous two cases plotted in a log–log scale. An additional case with $w/b = 2.5$ is also shown. The damping coefficients are observed to approach zero values with rapidly increasing slopes. Computationally, minimum damping values on the order of 10^{-20} were obtained, indicating that they are effectively zero-damping points. We note that these are points with finite added mass, thus similar to the waveless shapes mentioned in the Introduction.

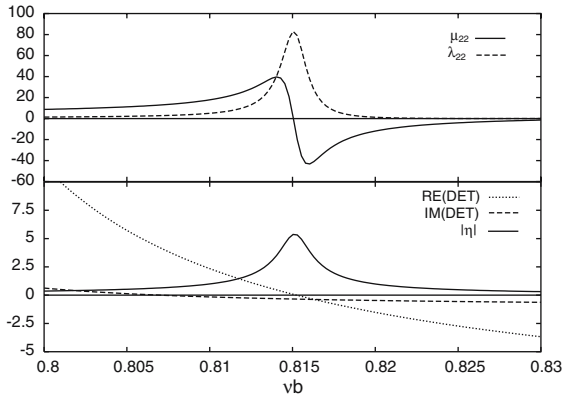

Fig. 4 Heave hydrodynamic coefficients at the first-order resonance, shown with determinant of (43) and (44) and wave elevation averaged over moonpool $|\bar{\eta}|$, $b/d = 1.0$, $w/b = 5.0$

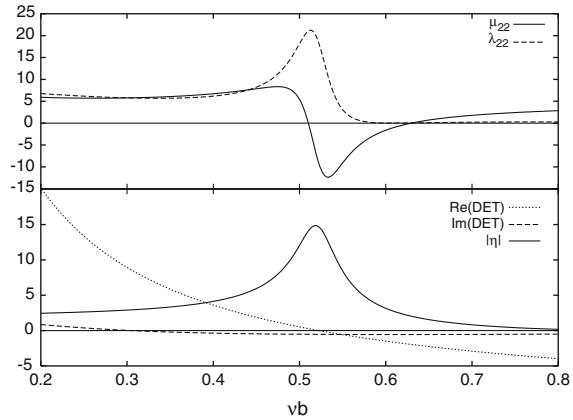

Fig. 5 Heave hydrodynamic coefficients at the Helmholtz resonance, shown with determinant of (43) and (44) and wave elevation averaged over moonpool $|\bar{\eta}|$, $b/d = 1.0$, $w/b = 1.5$

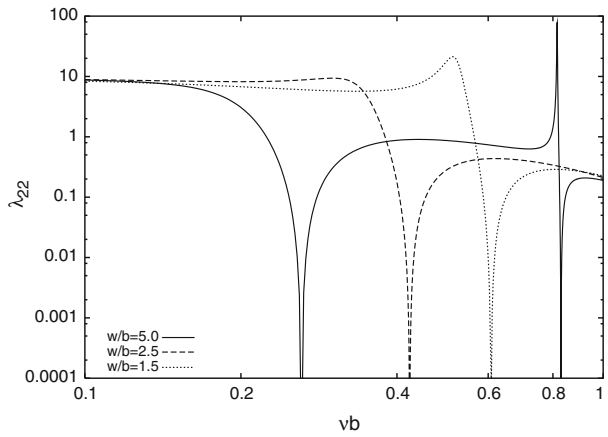

Fig. 6 Zero damping property for three moonpool widths: $w/b = 5.0, 2.5, 1.5$

3.2 Variation of hydrodynamic coefficients with moonpool width

It is of interest to examine the overall variation of the heave hydrodynamic coefficients with the moonpool width. For this purpose, w/b of the previous geometry is varied from 1.0 to 20. Figure 7 shows a contour plot of the (non-dimensional) added-mass coefficient μ_{22} with w/b and νb as variables. Figure 8 is the corresponding contour plot of the damping coefficient. For clarity, the damping coefficient is plotted in logarithmic scale, $\log_{10}\lambda_{22}$.

The loci of frequencies of each resonant mode show up clearly as dark lines on these plots. A dark shade indicates spiky values in the μ_{22} plot, but vanishing damping for the λ_{22} plot. As explained in the last section, the plots do not coalesce. The exception is the Helmholtz mode, which has a much larger bandwidth and is spread over a larger area at the bottom of each plot. The bandwidth of the higher-order resonance decreases as the order increases and becomes less noticeable. A significant difference between the Helmholtz mode and the other resonant modes is that, as the separation decreases to zero, this mode approaches a limiting frequency while the higher-order resonant frequencies tend toward infinity. This behavior is better understood by another plot.

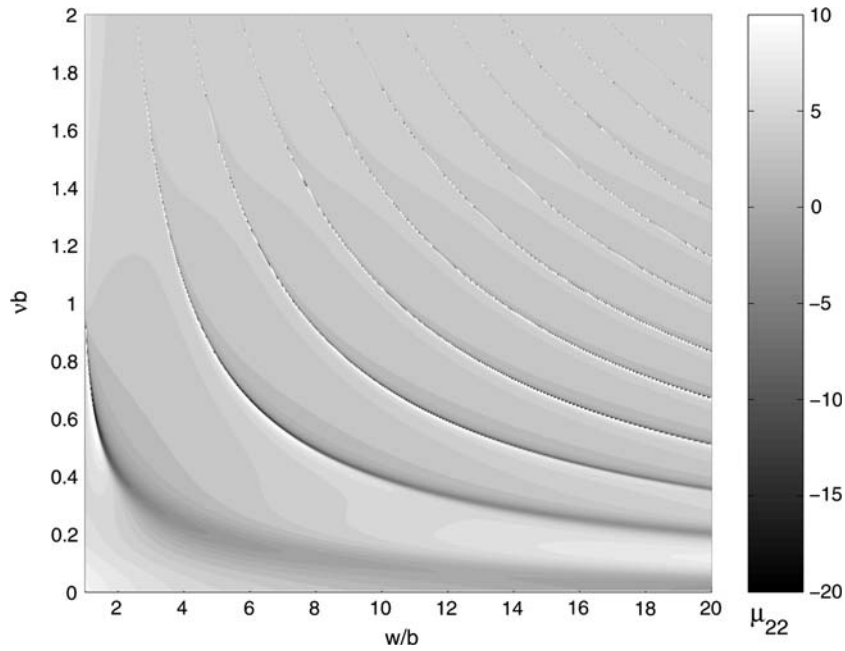

Fig. 7 Contours of μ_{22} with w/b and vb as variables, $b/d = 1$, $h/d = 20$

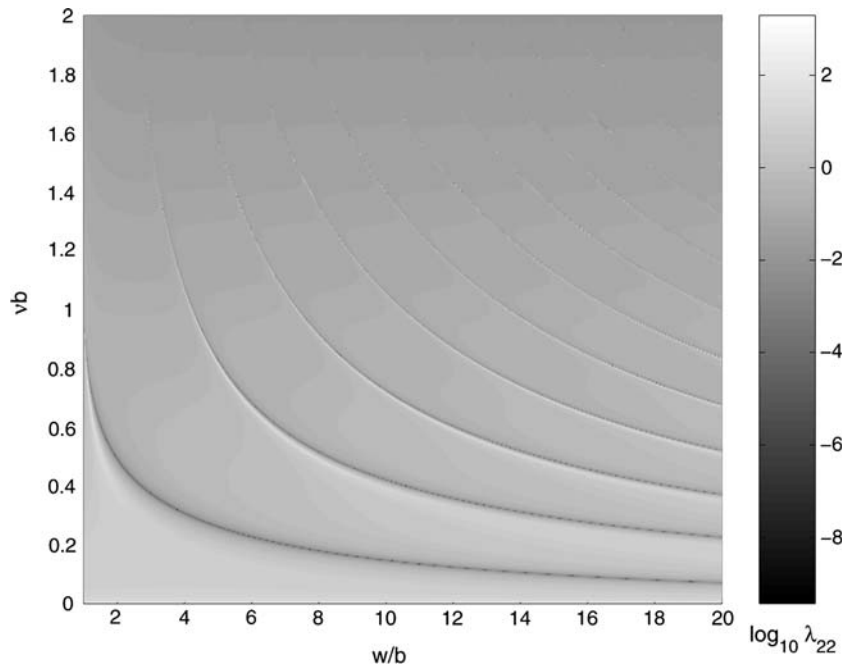

Fig. 8 Contours of λ_{22} with w/b and vb as variables, $b/d = 1$, $h/d = 20$

Figure 9 is a waterfall plot of the added-mass coefficients for increasing separations. The dashed line represents the single-body result ($w/b = 1.0$), which has no pumping mode present. Each w/b-value is plotted with a vertical translation ($\triangle$) of +3.45 units. The range of w/b shown is [1.0, 2.0], with an increment of 0.0345. The largest spike in the added-mass coefficient is marked by the solid line at $w/b = 1.01724$. The spike to the right of the largest one corresponds to $w/b = 1.01379$, which gradually diminishes to the single-body behavior. Faltinsen [24] gave an approximating formula for the Helmholtz frequency using a

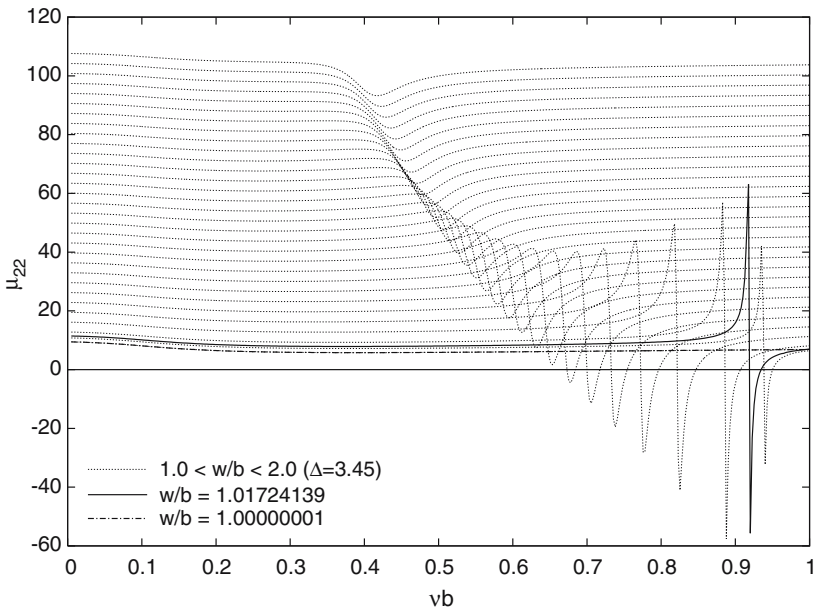

Fig. 9 Plot of μ_{22} versus νb for small moonpools, with $w/b =$ [1.0(0.0345)2.0], $d/b = 1.0, h/d = 20.0$

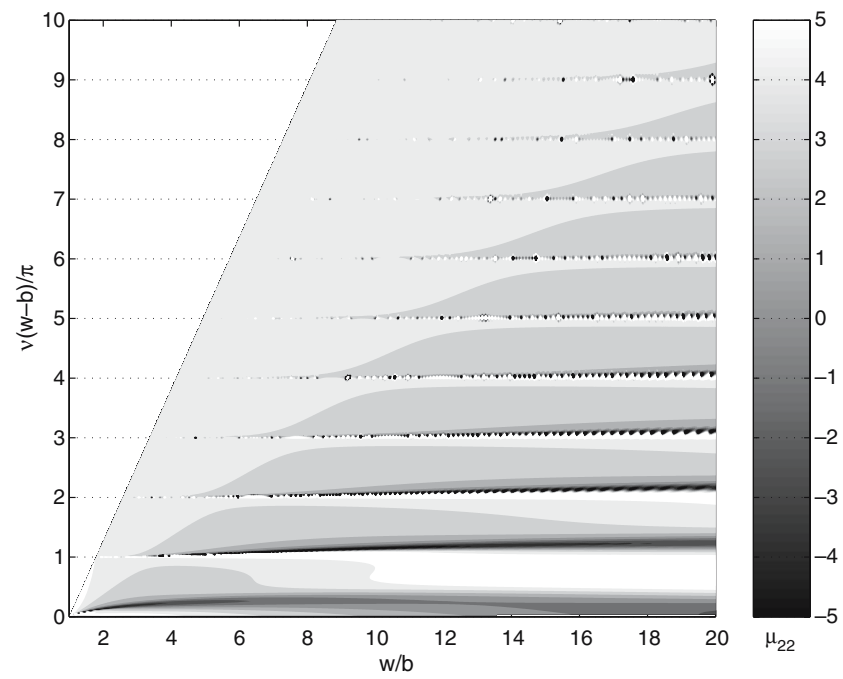

Fig. 10 Contours of μ_{22} plotted against w/b and $\nu(w-b)/\pi$

one dimensional U-tube analysis of the gap. In the present notation, his result suggests the resonance is at

$$\nu b = b/d. \tag{48}$$

The abscissa crossovers of μ_{22} in Fig. 9 correspond closely to the points of maximum motion. The present results suggest that (48) is only correct for very small gap ($w/b \approx 1.0$), and even so, the crossover point is less than b/d.

As w/b increases, μ_{22} eventually loses its spiky behavior with its positive spike decreasing in size, leaving a local minimum in the coefficient. Simultaneously, its Helmholtz-mode frequency also decreases gradually.

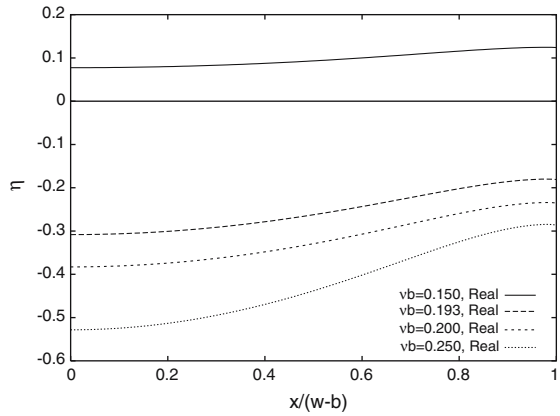

Fig. 11 Free-surface elevation, $\mathfrak{Re}\,\eta(x)$ in moonpool, from $\nu b = 0.15$ to 0.25, $w/b = 5.0$

Figure 10 is a plot of the heave added-mass coefficients against w/b and $\nu(w-b)/\pi$. It is clear that the higher-resonance modes occur close to frequencies that satisfy the following relation of standing waves:

$$\nu(w-b) = n\pi, \quad n = 1, 2, 3 \ldots \tag{49}$$

The first few (non-Helmholtz) resonant modes tend to occur at slightly lower values than $\nu(w-b)/\pi$ for the smaller gap widths. This is related to the fact that the oscillating waves sense the finiteness of the draft of the cylinders walls. The cylinder walls act as deep vertical walls at higher resonance frequencies when the standing waves are shorter. Thus the agreement with Eq. 49 would then be better.

4 Resonance free-surface shapes

With the definition of the potential given by (1), the spatial form of the free-surface elevation per unit motion ζ_2 is given by $\eta(x) = \nu\phi(x, 0)$, the real and imaginary parts of which are in phase and 90° out of phase, respectively, with the body displacement.

The geometry studied here is that of the twin cylinder in Fig. 2, with $b/d = 1$ and $h/d = 20$. It is helpful to keep in mind that the first three critical frequencies are numerically at $(\nu b)_0 = 0.2617$, $(\nu b)_1 = 0.829$, and $(\nu b)_2 = 1.577$.

4.1 Transiting across the Helmholtz mode

Figures 11 and 12 show $\mathfrak{Re}\,\eta(x)$ and $\mathfrak{Im}\,\eta(x)$, respectively, across the moonpool, $x = [0, w-b]$, for $\nu b = 0.15$ to 0.25. The profiles in these figures appear to be predominantly "piston-like", but with an appreciable sinusoidal component. The profiles for the maximum wave elevation at $\nu b = 0.193$ are also shown in these figures. It is interesting to note that, at this frequency, the spatial average of the imaginary component is larger than the real contribution. Additionally, the behavior of the profile closer to the zero-damping location can be observed in Fig. 13, as the frequency parameter traverses across $(\nu b)_0 = 0.2617$ from $\nu b = 0.260$ to 0.264. Here, $\mathfrak{Im}\,\eta(x)$ decreases uniformly to zero across the entire gap and then changes to an opposite (negative) phase. The vanishing of the $\mathfrak{Im}\,\eta(x)$ is consistent with the vanishing of the damping since a non-vanishing $\mathfrak{Im}\,\phi$ would have produced positive work on the fluid. Thus, at $(\nu b)_0$, ϕ is real and bounded, which is an interesting property.

4.2 Modal shapes at higher-order resonances

As can be seen from Fig. 14, when the frequency approaches the first higher-order critical frequency, at $(\nu b)_1 = 0.829$, there is a marked increase in the amplitude of $\mathfrak{Re}\,\eta(x)$. This is in agreement with the μ_{22} data

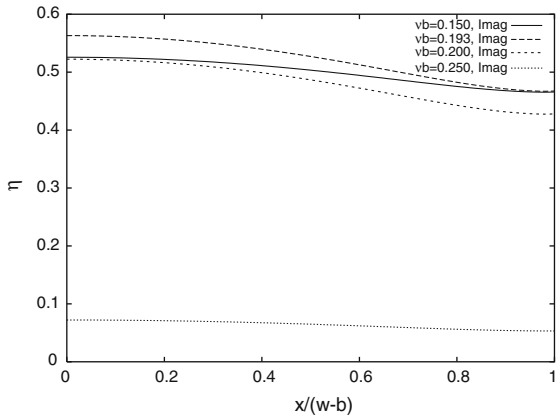

Fig. 12 Free-surface elevation, $\Im\mathfrak{m}\,\eta(x)$ in moonpool, from $\nu b = 0.15$ to 0.25, $w/b = 5.0$

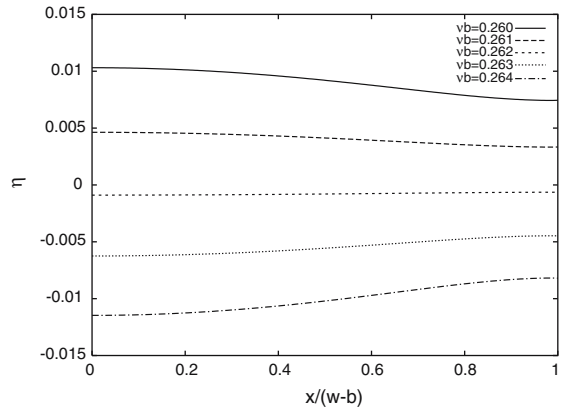

Fig. 13 Free-surface elevation, $\Im\mathfrak{m}\,\eta(x)$ in moonpool, across $(\nu b)_0 = 0.2617$

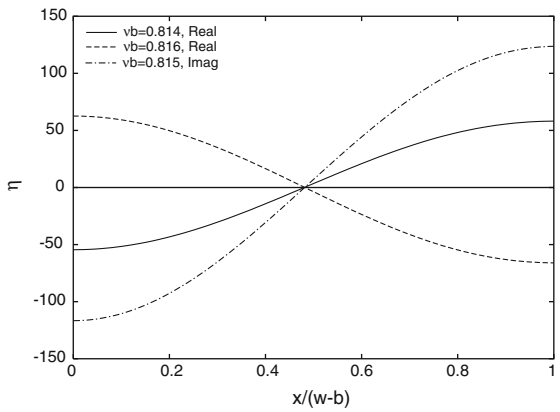

Fig. 14 Change in $\eta(x)$ across the first resonance frequency, $(\nu b)_1$

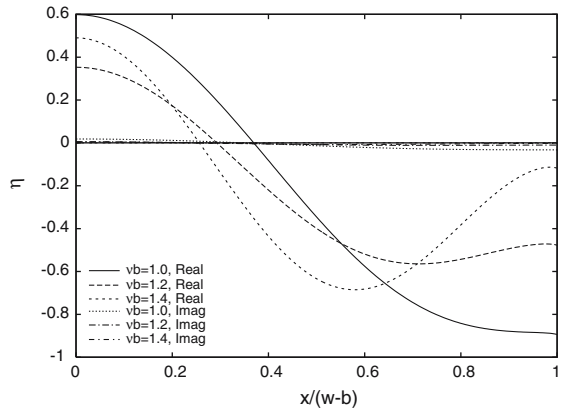

Fig. 15 Evolution of moonpool free-surface profile, $\eta(x)$, from $\nu b = 1.0$ to 1.4

as its value spikes up when it approaches the critical frequency. Close to $(\nu b)_1$, μ_{22} changes sign and the phase of the real wave profile rapidly flips, but the shape retains its half sinusoidal form in the half gap as shown in the figure. The two real components shown in this figure were taken at the positive and negative peaks of μ_{22}. A full standing wave is formed in the full moonpool space but added onto the constant $\Re\mathfrak{e}\,(B_0^{e1})$. At high frequencies, the imaginary component is usually comparably insignificant. However, with a spike in damping around the resonances, it is possible for the imaginary component of the wave profile to become dominant. An example of this is shown in Fig. 14 where the profile for this component is shown at the peak of λ_{22} with $\nu b = 0.815$. This also happens to be the case where the real component vanishes. Interestingly, while the real component undergoes a change in phase at this frequency, the imaginary component does not. Instead, the imaginary component changes phase at $(\nu b)_1 = 0.829$ ($\lambda_{22} = 0$), similar to the behavior in Fig. 13.

In contrast to the behavior preceding the first resonant frequency, as the frequency increases further beyond $(\nu b)_1$, the wave shape changes differently (Fig. 15). The minimum elevation at the body side moves inwards towards the center of the moonpool, while elevation at the cylinder wall increases. This behavior continues until the next resonance frequency near $(\nu b)_2$ is approached, near which the shape approaches that of a full sinusoid in the half-moonpool space (Fig. 16). Again, there is a marked increase in the magnitude of $\Re\mathfrak{e}\,\eta$ as this frequency is approached.

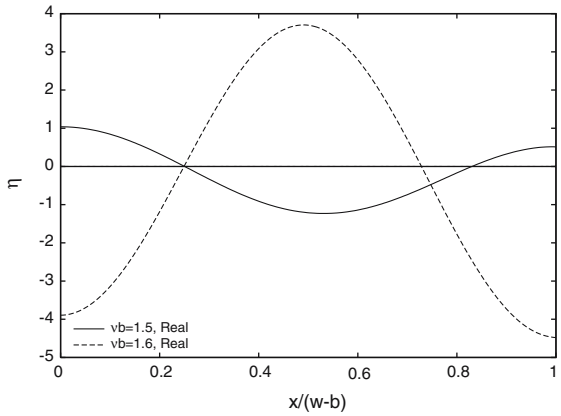

Fig. 16 Free-surface elevation, $\Re\mathrm{e}\ \eta(x)$, as frequency crosses the second resonance near $(\nu b)_2$

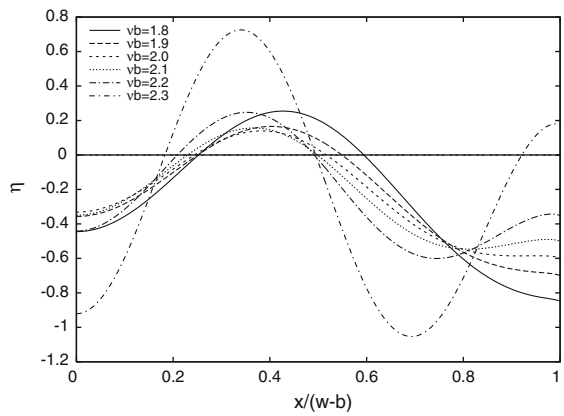

Fig. 17 Evolution of moonpool wave elevation $\Re\mathrm{e}\ \eta(x)$ from $\nu b = 1.8$ to 2.3

One can establish that this pattern of change repeats in a similar way as $(\nu b)_3 = 2.357$ is approached. It suffices to illustrate this by showing only $\Re\mathrm{e}\ \eta$ in Fig. 17, where the formation of *three* standing waves in the full moonpool width is imminent.

5 Conclusions

The problem of a heaving twin cylinder with a free-surface gap or moonpool was analyzed using an accurate, semi-analytical method, which is not plagued by irregular frequencies encountered in other formulations. Attention was directed to the occurrence of a sequence of critical frequencies at which the radiation damping vanishes. At frequencies slightly below each of these zero-damping points, $(\nu b)_i, i = 0, 1, 2 \ldots$, spiky behavior of the damping and added mass can occur. The magnitude of these intense variations, though never singular in reality for small i, depends on the body shape and other geometric ratios. Near $(\nu b)_0$ is the occurrence of the Helmholtz mode, where maximum moonpool motion can occur with a relatively flat, but not constant, wave profile. As the moonpool gap decreases, this resonant motion is more extreme or narrow-banded. The intensity of the moonpool motion is closely related to a spiky damping coefficient and a concurrent sign change in the heave added mass. As expected, a smaller moonpool width leads to a more piston-type behavior of the wave elevation.

In contrast to the Helmholtz oscillations, the higher-order resonances near the critical frequencies $(\nu b)_i, i = 1, 2, \ldots$, have been shown to be standing waves of integer wavelengths plus an additive constant in the moonpool region. The resonant motion takes place at frequencies close to a standing-wave formula based on moonpool width: $\nu(w - b) = n\pi,\ n = 1, \ldots$, which works well for short waves ($n \gg 1$), but becomes inaccurate as d/b decreases (shallower-draft cylinders).

Across a frequency of resonant motion, the following behavior of moonpool wave profile has been observed: The in-phase (or real) component relative to the cylinder displacement changes in sign, while the 90° out-of-phase (imaginary) component, usually the dominant component, remains at the same sign. The imaginary component does change in sign as the frequency traverses across $(\nu b)_n$. At these radiation-free points, the twin cylinder has finite added mass.

The present analysis is pertinent to time-domain simulations of motion of multiple-body systems in waves.

Acknowledgements We gratefully acknowledge the Office of Naval Research for partial support of this work under grant N00014-03-1-0211. The project was conducted under the auspices of the Consortium of Florida Atlantic University, under Award FAU #CRD66.

References

1. Wang S, Wahab R (1971) Heaving oscillations of twin cylinders in a free surface. J Ship Res 15(1):33–48
2. Marthinsen T, Vinje T (1985) Nonlinear hydrodynamic interaction in offshore loading systems. In: Proc 4th Int'l Conf on the Behaviour of Offshore Structures. Delft, The Netherlands, pp 293–302
3. Miles JW (1974) Harbor seiching. Ann Rev Fluid Mech 6:17–35
4. Miles JW, Lee YK (1975) Helmholtz resonance in harbors. J Fluid Mech 67:445–464
5. Ünlüata Ü, Mei CC (1975) Effects of entrance loss on harbor oscillations. J Waterways Harbors Coastal Engr Div ASCE 101:161–180
6. McIver M (1996) An example of non-uniqueness in the two-dimensional linear water wave problem. J Fluid Mech 315:257–266
7. McIver P, McIver M (1997) Trapped modes in an axisymmetric water-wave problem. Q J Mech Appl Math 50:165–178
8. Newman JN (1999) Radiation and diffraction analysis of the McIver toroid. J Engng Math 35:135–147
9. Motora S, Koyama T (1965) On wave-excitation free ship forms. Zosen Kiokai 117:115
10. Kyozuka Y, Yoshida K (1981) On wave-free floating-body forms in heaving oscillation. Appl Ocean Res 3(4):183–194
11. Garrett CJR (1970) Bottomless harbor. J Fluid Mech 43:433–449
12. Yeung RW (1981) Added mass and damping of a vertical cylinder in finite-depth waters. Appl Ocean Res 3(3):119–133
13. Miloh T (1983) Wave load on a solar pond In: Proc Int'l Workshop on Ship and Platform Motions. University of California Berkeley, pp 110–131
14. Shipway BJ, Evans DV (2003) Wave trapping by axisymmetric concentric cylinders. J Offshore Mech and Arctic Engng 125:59–64
15. Mavrakos SA (2004) Hydrodynamic coefficients in heave of two concentric surface-piercing truncated circular cylinders. Appl Ocean Res 26:84–97
16. Molin B (2001) On the piston and sloshing modes in moonpools. J Fluid Mech 430:27–50
17. Wehausen JV, Laitone EV (1960) Surface Waves. In: Handbuch der Physik vol IX. Springer Verlag pp 446–778
18. Yeung RW (1982) Hydrodynamic coefficients of several standard shapes. In: Memorandum of Computational Hydrodynamics Laboratory. Mass Inst of Tech Cambridge MA 5pp
19. Fotsch AR (1997) Inertia and damping of plates and blocks in finite-depth water. Graduate Student Paper. Society of Naval Architects and Marine Engineers, Nor-Cal Section, April 10
20. Bai KJ, Yeung RW (1974) Numerical solution to free-surface flow problems. In: Proc 10th Symp Naval Hydrodynamics. Cambridge, MA
21. Yeung RW, Newman JN (1977) Discussion on Paper by P. Sayer and F. Ursell "On the virtual mass, at long wavelengths, of a half-immersed circular cylinder heaving on water of finite depth" In: Proc 11th Symposium on Naval Hydrodynamics. Mech Engrg Publ Ltd., Inst of Mechanical Engineering, London pp 560–561
22. Bai KJ (1977) Added mass of two-dimensional cylinders heaving in water of finite depth. J Fluid Mech 81:85–105
23. Ursell F (1949) On the heaving motion of a circular cylinder in the free surface of a fluid. Quart J Mech Appl Math 2:218–231
24. Faltinsen OM (1990) Sea loads on ships and offshore structures. Cambridge University Press, Cambridge